EUROPEAN ORGANIZATION FOR NUCLEAR RESEARCH

MEASUREMENT OF STRUCTURE FUNCTIONS AND AZIMUTHAL CORRELATIONS IN LEPTON PAIRS PRODUCED IN TAGGED $\gamma\gamma$ COLLISIONS

L3 Collaboration

Abstract

The reaction $e^+e^- \to e^+e^-l^+l^-$ in a single tag configuration, has been studied at LEP with the L3 detector for $l = e, \mu$ using 93.7 pb^{-1} of data collected from 1991 to 1994. Various differential cross-sections have been measured for $1.4 < Q^2 < 7.6$ GeV^2. The F_2^γ photon structure function has been extracted for $l = \mu$. Azimuthal correlations related to other other leptonic structure functions of the photon have also been measured.

Submitted to *International Europhysics Conference on High Energy Physics, EPS97, Jerusalem.*

1 Introduction and Formalism

Detectors at e^+e^- colliders are well suited for investigating photon-photon collisions. Due to the growth of the photon emission probability with the beam energy, the cross-section for the two-photon process is much higher at LEP than in any previous e^+e^- collider.

The reaction $e^+e^- \rightarrow e^+e^-\gamma\gamma \rightarrow e^+e^-l^+l^-$ in a single tag configuration (where l can be any charged lepton) arises from QED $O(\alpha^4)$ processes [1] and can be seen as an $e-\gamma$ deep inelastic scattering. This framework provides not only a QED test but also an experimental check for the procedures adopted in the study of the photon hadronic structure functions.

Using the data collected from 1991 to 1994 with the L3 experiment at LEP, we have investigated the deep inelastic $e-\gamma$ scattering (DIS) and we report here our results on the leptonic reactions:

$$e\gamma \rightarrow e + e^+ + e^-,$$

$$e\gamma \rightarrow e + \mu^+ + \mu^-,$$

where the three final leptons are detected and γ is an almost real virtual photon radiated by the untagged electron. The analysis of the structure functions has been applied only to the $\mu^+\mu^-$ channel.

The lowest order Feynman diagrams which describe the reactions $e^+e^- \rightarrow 4$ leptons can be classified as: multiperipheral, annihilation, bremsstrahlung, conversion (Fig. 1). In the single-tag configuration and in the observed range of di-lepton mass $W_{\gamma\gamma}$ ($W_{\gamma\gamma} > 0.5\ GeV$), the dominant contribution is the multiperipheral diagram, which involves the two-photon interaction (see Tab. 1). For small masses Annihilation and Bremsstrahlung contributions become important.

We have analysed the reaction $e^+e^- \rightarrow e^+e^-\gamma\gamma \rightarrow e^+e^-l^+l^-$ where only one of the scattered electrons is detected at a polar angle greater than 1.55^o from the beam axis while the other (anti-tag) goes undetected along the beam pipe.

In the deep inelastic scattering formalism, the variables which describe these events are defined in the following way (Fig. 2):

$k_1,\ k_2$		: probe and target photon four-momenta,
Q^2	$= -k_1^2;\ t^2 = -k_2^2$	: virtualities of the photons,
$W_{\gamma\gamma}^2$	$= (k_1 + k_2)^2$	: invariant mass squared of the produced lepton pair,
$x_{1,2}$	$= \frac{k_{1,2}^0}{E_{beam}} = \frac{E_{1,2}^\gamma}{E_{beam}}$	: energy fraction of the photon relative to the beam energy,
$\frac{dn(x_2)}{dx_2}$		: target photon flux,

and

$$x = \frac{Q^2}{2k_1k_2} = \frac{Q^2}{Q^2+W^2}; \qquad y = \frac{k_2k_1}{k_2p_1} \simeq 1 - \frac{E_1^\gamma}{E_{beam}}\cos^2\frac{\theta}{2} \simeq 1 - x_1$$

are the standard Bjorken scaling variables.

The cross-section for deep-inelastic electron scattering on a photon target can be written in terms of the sum of the contributions of transverse (T) and longitudinal (L) photons. For the single tag configuration, one has [1,2]:

$$\frac{d^3\sigma}{dxdQ^2dx_2} = \frac{4\pi\alpha^2}{Q^4}\frac{1}{x}\frac{dn(x_2)}{dx_2}\left\{[(1-y+\frac{y^2}{2})]F_2^\gamma(x,Q^2)+\frac{y^2}{2}F_L^\gamma(x,Q^2)\right\} \tag{1}$$

where

$$F_T^\gamma \propto \sigma_{TT};\ F_L^\gamma \propto \sigma_{TL} \text{ and } F_2^\gamma = 2xF_T^\gamma + F_L^\gamma$$

F_2^γ, F_L^γ and F_T^γ are the photon structure functions which are proportional to the cross-sections σ_{ij} for transversely and longitudinally polarised virtual photons (the first index refers to the target photon while the second index refers to the probe photon). In the present analysis, y^2 is very small ($y^2 < 4.5 \cdot 10^{-4}$), so that the measurement of the differential cross-section is sensitive only to F_2^γ. By neglecting terms of the order of m_l^2/Q^2 and expressing Q^2 in terms of $W^2$and t^2, the QED prediction for the photon structure function F_2^γ is [2]:

$$F_2^\gamma(x,t^2,W^2) = \frac{\alpha}{\pi}x\left\{[x^2+(1-x)^2]ln\frac{W^2}{m_l^2+t^2x(1-x)} - 1 + 8x(1-x) + \frac{t^2x(1-x)}{m_l^2+t^2x(1-x)}\right\} \tag{2}$$

The contribution of the amplitudes for longitudinally polarised photons may be observed by measuring angular correlations in the $\gamma\gamma$ centre of mass [2–5]. In a single-tag configuration, assuming that the target photon direction is parallel to the beam axis, two independent angles can be defined in the $\gamma\gamma$ centre of mass system(Fig. 3). θ^* is the polar angle between the μ^- and the $\gamma\gamma$. χ is the azimuthal angle between the planes defined by the two-body final state and the $\gamma\gamma$ axis, and the scattering plane of the tagged electron. The decomposition of the cross-section into the contributions from the different photon helicity amplitudes leads to a formula with 13 terms each having a different azimuthal dependence. In the single-tag configuration, neglecting the longitudinal component of the target photon, only three terms remain in the cross-section formula which can be written as [4]:

$$\frac{d^4\sigma}{dxdydzd\chi} = \frac{2\pi\alpha^2}{Q^2}\frac{1+(1-y)^2}{xy}[A_1(x,z)+A_2(x,z)\cdot cos(\chi)+A_3(x,z)\cdot \cos(2\chi)] \tag{3}$$

where $z = cos(\theta^*)$ and A_1 is the sum of the amplitudes squared of the helicity states while A_2 and A_3 are the interference terms leading to the $cos(\chi)$ and $cos(2\chi)$ modulation [3]. The coefficients A_i are known QED functions which can be expressed in good approximation[1)] as follows [2,4,5]:

$$\begin{aligned} A_1 &\simeq \tfrac{x\alpha}{\pi}\left([x^2+(1-x)^2]\tfrac{1+(\beta z)^2}{1-(\beta z)^2}+4x(1-x)\right) \\ A_2 &\simeq -\tfrac{4\alpha}{\pi}x(1-2x)\sqrt{x(1-x)}\tfrac{z}{\sqrt{1-(\beta z)^2}} \\ A_3 &\simeq \tfrac{2\alpha}{\pi}x^2(1-x) \end{aligned} \tag{4}$$

and $\beta = \sqrt{1-4xm_l^2/[Q^2(1-x)]}$.

[1)]The symbol $\simeq$ used in Eq. 4 indicates that $\gamma\gamma$ luminosity functions $\propto 1-y$ have been set to one. Also it is assumed that the target photon is purely transverse. Note that the formulae in Ref. [5] are incorrect.

The coefficients A_1, A_2, A_3 can be expressed in terms of three differential structure functions $\overline{F}_2^\gamma, \overline{F}_A^\gamma, \overline{F}_B^\gamma$, according to the relations[2)] [4]:

$$\begin{array}{lcl} A_1 & \simeq & \overline{F}_2^\gamma(x,z) = 2x\overline{F}_T^\gamma(x,z) + \overline{F}_L^\gamma(x,z) \\ A_2 & \simeq & -\overline{F}_A^\gamma(x,z) \\ A_3 & \simeq & \frac{1}{2}\overline{F}_B^\gamma(x,z) \end{array} \tag{5}$$

Since A_2 comes from the interference between longitudinal and transverse photons (Fig. 4), it is sensitive to the amplitude with total photon helicity $\lambda = 1$ whose square is the well known longitudinal structure function. The interference between two transverse photons is described by $A_3 \propto F_B^\gamma$. It must be noted that F_L^γ and F_B^γ are the same functions of x and z (and, in the literature both typically referred to as 'F_L^γ') but their helicity structures are different. Indeed, F_B^γ is purely transverse. Since the longitudinal structure function F_L^γ appears in the cross-section formula (Eq. 1) multiplied by the small factor y^2 it is difficult to measure. The azimuthal coefficient A_2 has no such suppression factor and therefore it gives access to the same amplitude with improved experimental sensitivity.

2 Monte Carlo Simulation

To calculate the selection efficiencies and backgrounds and to compare the data to the QED predictions, two Monte Carlo generators, together with a full detector simulation, have been used: the Berends, Daverdveldt and Kleiss (BDK) generator [8] and the Vermaseren [9] generator. The former, which calculates to $O(\alpha^4)$ the full set of QED diagrams taking into account interference effects, has been used as a reference[3)] while the second, which is much faster since it has exact calculations only for multiperipheral diagram, has been used to produce large statistics Monte Carlo event samples. None of these generators simulates the initial state radiation. To check the influence of the initial state radiation on our results we have also used a Monte Carlo generator developed by F.A. Berends and P.H. Daverdveldt [10, 11] which simulates the process $e^+e^- \longrightarrow e^+e^-\mu^+\mu^-(\gamma)$.

For all the generated samples, the events were simulated and reconstructed in the full L3 detector and passed through the same analysis chain as the real data.

3 Data selection

The data have been collected at the Z peak running period with the L3 detector. The detailed description of the L3 detector can be found elsewhere [6]. The analysis described in this paper is mainly based on the charged particle central tracker, the electromagnetic (EM) and the hadron calorimeter. Two cylindrical electromagnetic calorimeters, the Luminosity Monitors, situated at $\simeq 2.7\ m$ away from the interaction point, allow electron tagging in the region $1.4^o \leq \theta \leq 3.9^o$ and $176.1^o \leq \theta \leq 178.6^o$.

Only events with a total energy deposit in the electromagnetic calorimeters smaller than 60 GeV are considered in order to eliminate events from Z decay.

In the luminosity monitors the tag is defined as a single shower energy deposit $E_{EM} \geq 0.75 \cdot E_{beam}$ lying inside the fiducial region ($1.55^o < \theta < 3.67^o$ and $176.3^o \leq \theta \leq 178.5^o$) which

[2)]The usual structure functions F_2^γ, F_A^γ and F_B^γ are recovered by integrating $\overline{F}_i^\gamma$ over z.

[3)]In the BDK program, large angle tagging cuts can only be put in by hand, i.e. by throwing away those events that do not satisfy the cuts, reducing considerably the efficiency in this application.

excludes the innermost and outermost crystals of the detector. Single-tag events are selected by imposing that no other electron with $E_{EM} \geq 0.75 \cdot E_{beam}$ is seen in the whole L3 detector.

The lepton pair is selected by requiring two well measured tracks with opposite charges. The two tracks are required to lie inside a fiducial region of $28^\circ \leq \theta \leq 152^\circ$, with a maximum distance of closest approach from the nominal vertex of 10 mm and a transverse momentum $p_t > 0.1GeV$.

The electrons and muons are then identified by comparing the momentum measured by the tracking chamber with the electromagnetic energy and using hadron calorimeter information. For a well identified electron we require that:

- the ratio $R = E_{EM} \sin\theta / p_t$ must be greater than 0.8 in the barrel region $44^\circ \leq \theta \leq 136^\circ$ and $E_{EM} \geq 0.4GeV$
- R must be greater than 0.7 in the endcap region and $E_{EM} \geq 0.6\ GeV$. The differences between the cuts are due to the less accurate measurements in the endcap regions.

To select muon pairs we require:

- at least one energy deposit in the hadronic calorimeter associated with a selected track.
- at least one energy deposit of less than 0.40 GeV in the electromagnetic calorimeters associated with the selected tracks. The deposit of a minimum ionising particle is in average 0.22 GeV. Moreover more than 95 % of the measured energy must be contained in at most 6 crystals.

For both e^+e^- and $\mu^+\mu^-$ pairs only one well identified particle is required , in order to cover uniformly the angular range defined by the tracks. In the e^+e^- sample both electrons are identified in 76% of the events. In the $\mu^+\mu^-$ sample both muons reach the hadron calorimeter in 40 % of the events, and in 80% of the events both particles give a signal consistent with a minimum ionising particle. From the measured particles the kinematics of the final state can be reconstructed, giving an indirect measurement of the missing untagged electron.

The $\gamma\gamma$ events with a tagged electron detected in the luminosity monitors are mainly collected by the energy trigger requiring an energy deposit greater than 30 GeV in the luminosity monitor and at least one track in the central tracking chamber with a transverse momentum $p_t > 0.1GeV$. Other triggers [6,7] can be activated by the same event and allow the triggering efficiency to be monitored. The trigger efficiencies have been studied for each year. Since the trigger multiplicity, i.e. the number of independent triggers for a given event, is often greater than one, it has been possible to perform a careful study of the trigger efficiency. The trigger efficiency has been found independent of the invariant mass $W_{\gamma\gamma}$. A mean inefficiency of 1.3% for the electron channel and 2.7% for the muon channel has been found. The periods in which some detector and trigger instabilities were evident have been excluded from the sample of data. The selection criteria were applied to the data collected from 1991 to 1994 corresponding to a total integrated luminosity of 93.7 pb^{-1}.

The number of selected events, for both channels, are reported in Tab. 2 together with the Monte Carlo expectations. In the radiative Z decays, $Z \longrightarrow l\bar{l}\gamma$, the emitted photon can fake the tagged electron, but less than 1% of the radiated photons have an energy greater then 30 GeV and the single-tag condition makes this background negligible. The radiative $Z \longrightarrow q\bar{q}\gamma$ decay has been studied and the contribution to the background has also been find to be negligible. The contribution to the background from other $\gamma\gamma$ inclusive channels has been studied. The background contributions are summarised in Tab 3. We found an overall background contribution of less than 1% for the electron channel and of 1.8% for the muon channel.

The selection efficiencies for both e^+e^- and $\mu^+\mu^-$ channels as function of Q^2 are shown in Fig. 5. The difference observed in the selection efficiency between muons and electrons is due to the lower cut on the electromagnetic energy used to discriminate electrons and muons.

In Fig. 6 we show respectively the experimental distributions of the effective mass $W_{\gamma\gamma}$ and $cos(\theta)$ for the electron and muon pairs: the shape of all distributions is in a good agreement with the Monte Carlo expectations.

4 Results

The differential cross-sections $d\sigma/dQ^2$ are shown in Fig. 7 for $1.4 < Q^2 < 7.6\ GeV^2$ and $W_{\gamma\gamma} > 0.5\ GeV$ together with the analytical curves obtained from Eq. 1 using the Weizsäcker-Williams approximation for the target photon flux [1]. Notice that in this high Q^2 and high mass range the e^+e^- and $\mu^+\mu^-$ cross-sections are of the same order of magnitude.

Systematic uncertainties from the background and from the energy trigger efficiency have been estimated to be 3.2% for the di-muon channel and 1.6% for the di-electron channel.

4.1 Determination of F_2^γ

The measured cross-section is related to the structure function F_2^γ by the relation (neglecting terms in y^2 in Eq. 1):

$$F_2^\gamma(x, Q^2) = < \frac{1}{K(x, Q^2)} > \cdot \frac{d^2\sigma}{dx dQ^2}$$

where

$$K(x, Q^2) = \frac{\pi\alpha^2}{E_{beam}^2 Q^4 x} \int_{x_2^{min}}^{x_2^{max}} (1 - \frac{W^2 + Q^2(1 - x_2)}{x_2}) \frac{dn(x_2)}{dx_2} dx_2. \qquad (6)$$

The average correction factor $< 1/K(x, Q^2) >$, for each bin in x and Q^2, is calculated by Monte Carlo integration using the generated events and Eq. 6. The value of F_2^γ obtained in $\gamma\gamma \rightarrow \mu^+\mu^-$ channel is shown in Fig. 8.

The effects of the target photon vituality have been analysed. If the target photon is considered real ($t^2 = 0$) the QED prediction for F_2 is significantly higher than the measured values. By fitting the experimental results with Eq. 2 we obtain a mean value for the virtuality t^2 of the target photon of $0.033 \pm 0.005\ GeV^2$ which is in very good agreement with the value of $0.034 \pm 0.002\ GeV^2$ obtained from the Berends-Kleiss Monte Carlo with radiative corrections [10, 11]. These results should be taken into account in studying the hadronic structure functions of the photon and indicate that theoretical parametrisations of parton density functions should take properly into account the virtuality of the target photon.

4.2 Azimuthal Correlations

The azimuthal correlations are analysed for the $\mu^+\mu^-$ single-tag sample. The kinematical configuration in the $\gamma\gamma$ centre of mass frame is completely determined by the two outgoing muons. To compute the angle θ^* the beam axis is taken as the target photon direction.

The experimental χ distributions have been fitted using a function of the form:

$$\frac{dN}{d\chi} = C \cdot [1 + R_\chi cos(\chi) + R_{2\chi} cos(2\chi)] \qquad (7)$$

with R_χ, $R_{2\chi}$ and C as free parameters. From Eq. 4 and Eq. 5 it follows: $C \propto F_2^\gamma$, $R_\chi \propto F_A^\gamma/F_2^\gamma$ and $R_{2\chi} \propto F_B^\gamma/F_2^\gamma$.

To analyse the evolution in x of R_χ and $R_{2\chi}$ we have used four intervals: $0 < x < 0.25$, $0.25 < x < 0.5$, $0.5 < x < 0.75$ and $0.75 < x < 1$. Since F_A^γ is antisymmetric in z, we have studied the x dependence of R_χ in two different ranges of z: $-0.7 < z < 0$ and $0 < z < 0.7$. While, to determine the x dependence of $R_{2\chi}$ we have used the full range $-0.7 < z < 0.7$ and in this case R_χ vanishes. The z ranges do not extend up to ± 1 in order to minimise the systematic instabilities related to this cut.

The azimuthal distributions obtained from the data and corresponding to the different x and z ranges are reported in Fig. 9 and in Fig. 10.

Different sources of systematic errors have been taken into account. We have tested the influence on the determination of χ of Q^2 and muon momentum resolutions. We find a systematic deviation on the determination of the ratios R_χ and $R_{2\chi}$ of 20%. Moreover an additional 4% effect as been found to be due to radiative corrections. The effects of cuts on z and x has been found to contribute less than 3% to the systematic error.

The acceptance and efficiency corrections have been applied in two independent ways: by applying a bin-to-bin correction determining acceptances from generated and reconstructed Monte Carlo, and using different unfolding algorithms [12, 13]. Since the extraction of the azimuthal distributions is strongly affected by the detector effects corrections, unfolding gives a method to obtain a less biased solution and helps to estimate the systematic errors. From the average deviation, we deduce a systematic error coming from the correction method of $< 1\%$ for R_χ and 13% for the determination of $R_{2\chi}$. The experimental values of R_χ and $R_{2\chi}$ are summarised in Tab. 4 and Tab. 5. The comparison with the QED predictions is shown in Fig. 11.

The measured values for R_χ and $R_{2\chi}$ are significantly different from zero and compatible with the theoretical expectations. The evolution of the ratio $R_{2\chi}$ with the scaling variable x has already been measured by the OPAL [15] collaboration in a wider range of z, nevertheless since A_1 depends on the cut applied on z, a correction factor is needed to compare these two measurements.

To extract the structure functions F_A and F_B from the experimental determination of the evolution of R_χ, $R_{2\chi}$ and F_2^γ with the scaling variable x the effect of the cut on z must be corrected. A set of correction factors C_{R_χ} and $C_{R_{2\chi}}$ have been computed. Comparing the theoretical values of the ratios R_χ and $R_{2\chi}$ obtained by numerical integration of equations 4 over the full interval of z with the result obtained integrating over $-0.7 \leq z \leq 0.7$ the correction factors reported in Tab. 6 have been obtained. The structure functions F_A and F_B are then extracted as follows:

$$F_B = 2C_{R_{2\chi}} R_{2\chi} F_2^{\gamma\gamma}$$

$$F_A = \frac{1}{2} C_{R_\chi} R_\chi F_2^{\gamma\gamma}$$

where $F_2^{\gamma\gamma}$ correspond to the experimental determination reported in this paper. The evolution of the structure functions F_A and F_B with the scaling variable x together with the QED expectations are reported in Fig 12.

The structure function F_A, being sensitive to $\lambda = 1$ helicity amplitude, helps to infer information about the longitudinal structure function of the photon.

5 Conclusions

We have analysed the two-photon reaction $e^+e^- \longrightarrow e^+e^-l^+l^-$ $(l = e, \mu)$ using data collected during the 1991 to 1994 L3 running period. By using the di-muon final state in two-photon collisions, we have extracted the leptonic structure function F_2^γ from the observed $d\sigma/dxdQ^2$ cross-section distribution. The effect of the virtuality of the target photon on the determination of the structure function has been studied. The distribution of F_2^γ as function of x differs of 10% from the analytical expectation obtained by neglecting the virtuality of the target photon. By fitting the experimental data with the analytical formula of F_2^γ with the target photon virtuality as a free parameter we found a mean value of $t^2 = 0.033 \pm 0.005\ GeV^2$ which is in very good agreement with the Monte Carlo expectation. The study of azimuthal distributions in the $\gamma\gamma$ centre of mass frame has enabled the measurement of F_A and F_B structure functions. The former is sensitive to the $\lambda = 1$ helicity amplitude that appears into the longitudinal photon structure function.

6 Acknowledgements

We wish to thank F.A. Berends and G.A. Schuler for the useful discussions. We thank G. d'Agostini for the interesting discussions on the unfolding procedures. We express our gratitude to the CERN accelerator divisions for the excellent performance of the LEP machine.

References

[1] V.M. Budnev *et al.*, *Phys. Rep.* C **15**, 181 (1975).

[2] H.J. Behrend *et al.*, *Phys. Lett.* B **126**, 384 (1983).

[3] P. Kessler in *Photon '95*, ed. J. Miller (World Scientific, Singapore, 1995).

[4] J.H. Field, summary talk in *Photon '95*, ed. J. Miller (World Scientific, Singapore, 1995).

[5] C. Peterson *et al.*, *Nucl. Phys.* B **229**, 301 (1983).

[6] B. Adeva *et al.*, *Nucl. Instrum. Methods* A **289**, 35 (1990).

[7] R. Bizzarri *et al.*, *Nucl. Instrum. Methods* A **317**, 463 (1992)

[8] F.A. Berends *et al.*, Comp. Phys. Comm. **40**, 285 (1986).

[9] J.A.M. Vermaseren, *Nucl. Phys.* B **229**, 347 (1983).

[10] F.A. Berends *et al.*, Comp. Phys. Comm. **40**, 271 (1986).

[11] F.A. Berends *et al.*, *Nucl. Phys.* B **253**, 421 (1985).

[12] G. D'Agostini, *Nucl. Instrum. Methods* A **362**, 487 (1995).

[13] A. Höcker and V. Kartvelishvili, CERN Preprint hep-ph/9509307.

[14] J. Boyer *et al.*, *Phys. Rev. Lett.* **56**, 207 (1986).

[15] K. Ackerstaff *et al.*, *CERN-PPE/96-153.*

Main Cuts	Channel	$\sigma_{multiper.}$(nb)	$\sigma_{ann.}$(nb)	$\sigma_{bremss.}$(nb)	$\sigma_{conv.}$(nb)
$\theta_{tag} > 24mrad$ $\theta_{\mu} > 25^{o}$ $W_{\gamma\gamma} > 0.5GeV$	$ee\mu\mu$	0.21 ± 0.002	$< 10^{-4}$	$0.13 \cdot 10^{-2} \pm 0.3 \cdot 10^{-3}$	$< 10^{-3}$

Table 1: Cross-sections for QED processes contributing to the reaction $e^+e^- \longrightarrow e^+e^-\mu^+\mu^-$ in a single tag configuration.

Process	Selected Events	Expected from MC
$ee\mu\mu$	7202 ± 85	7119 ± 84
$eeee$	3801 ± 63	3842 ± 62

Table 2: Number of selected events (background subtracted) compared to the MC expectations.

Background	Channel	
	$\gamma\gamma \longrightarrow e^+e^-$	$\gamma\gamma \longrightarrow \mu^+\mu^-$
$Z \longrightarrow \mu^+\mu^-\gamma$	—	—
$\gamma\gamma \longrightarrow e^+e^-$	—	0.78%
$\gamma\gamma \longrightarrow \tau^+\tau^-$	0.9%	0.71%
$\gamma\gamma \longrightarrow u\overline{u}$	< 0.1%	0.32%
Total	0.9%	1.8%

Table 3: Expected background contributions.

Δx	Δz	R_χ
0 – 0.25	0 – 0.7	$0.30 \pm 0.06 \pm 0.06$
0.25 – 0.5	0 – 0.7	$0.10 \pm 0.07 \pm 0.05$
0.5 – 0.75	0 – 0.7	$-0.21 \pm 0.09 \pm 0.04$
0.75 – 1	0 – 0.7	$-0.20 \pm 0.07 \pm 0.05$
0 – 0.25	-0.7 – 0	$-0.22 \pm 0.07 \pm 0.05$
0.25 – 0.5	-0.7 – 0	$-0.07 \pm 0.07 \pm 0.06$
0.5 – 0.75	-0.7 – 0	$0.16 \pm 0.09 \pm 0.06$
0.75 – 1	-0.7 – 0	$0.19 \pm 0.08 \pm 0.08$

Table 4: Azimuthal correlations: R_χ for the different x ranges. Results shows also the antisymmetry in z.

Δx	Δz	$R_{2\chi}$
$0 - 0.25$	-0.7 – 0.7	$0.24 \pm 0.06 \pm 0.06$
$0.25 - 0.5$	-0.7 – 0.7	$0.35 \pm 0.06 \pm 0.12$
$0.5 - 0.75$	-0.7 – 0.7	$0.38 \pm 0.07 \pm 0.13$
$0.75 - 1$	-0.7 – 0.7	$0.16 \pm 0.05 \pm 0.08$

Table 5: Azimuthal correlations: $R_{2\chi}$ for the different x ranges.

Δx	$C_{R_{2\chi}}$	C_{R_χ}
$0 - 0.25$	0.1933	0.6118
$0.25 - 0.5$	0.3184	1.0185
$0.5 - 0.75$	0.3715	1.1368
$0.75 - 1$	0.3812	1.2089

Table 6: Theoretical factors used to correct the effect of the z cut on the determination of R_χ and $R_{2\chi}$.

List of Figures

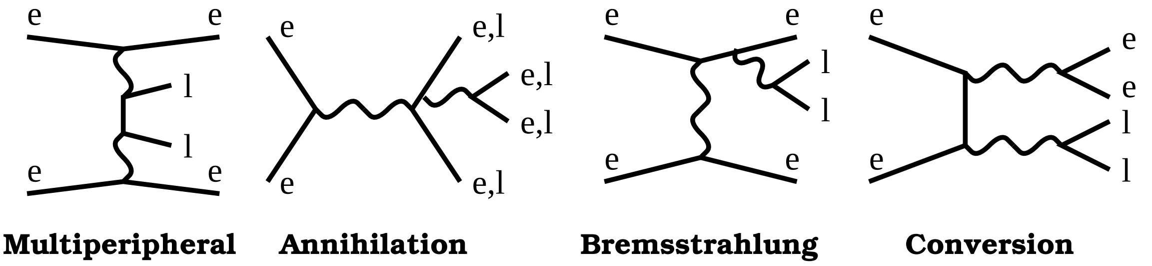

Figure 1: Examples of lowest order diagrams describing the reaction $e^+e^- \longrightarrow e^+e^-l^+l^-$.

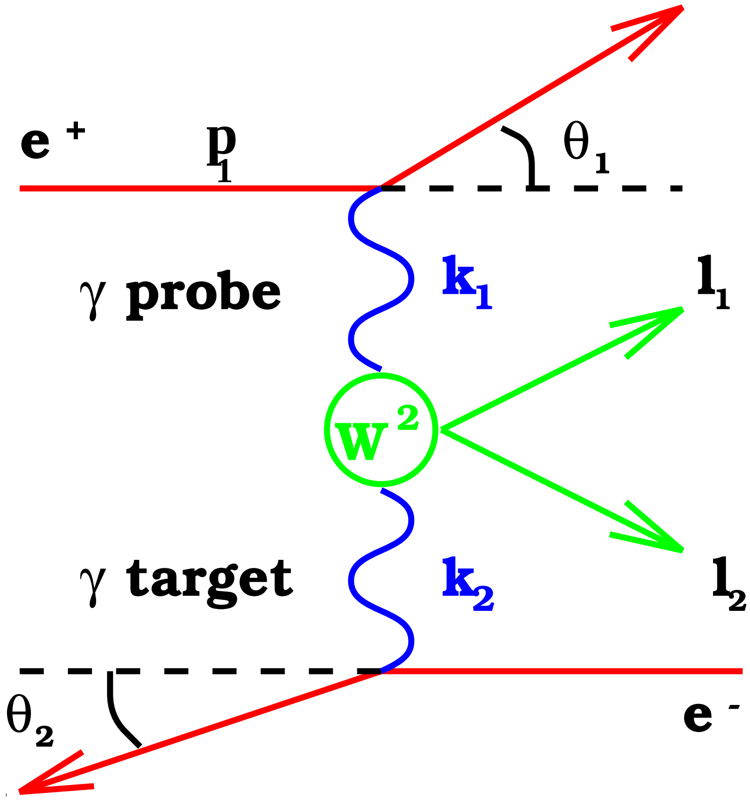

Figure 2: Definition of kinematical variables.

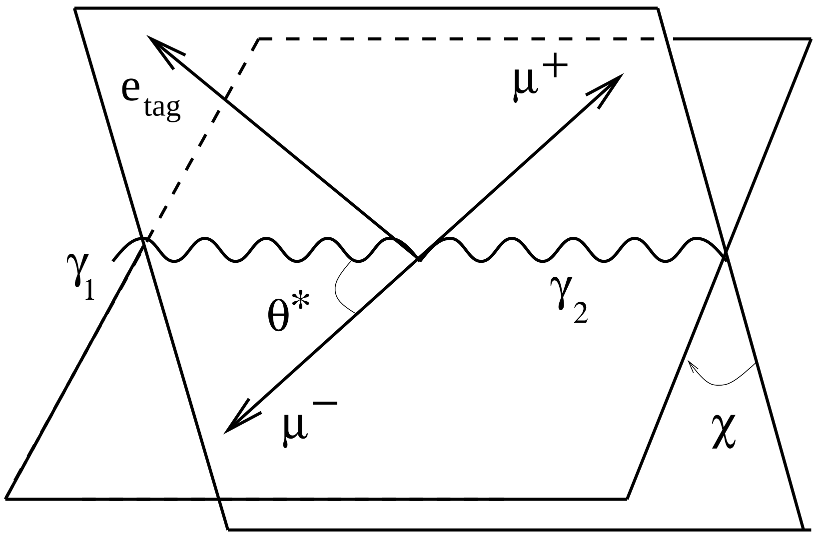

Figure 3: Definition of angles in the $\gamma\gamma$ centre of mass frame, used in the analysis of the azimuthal correlations.

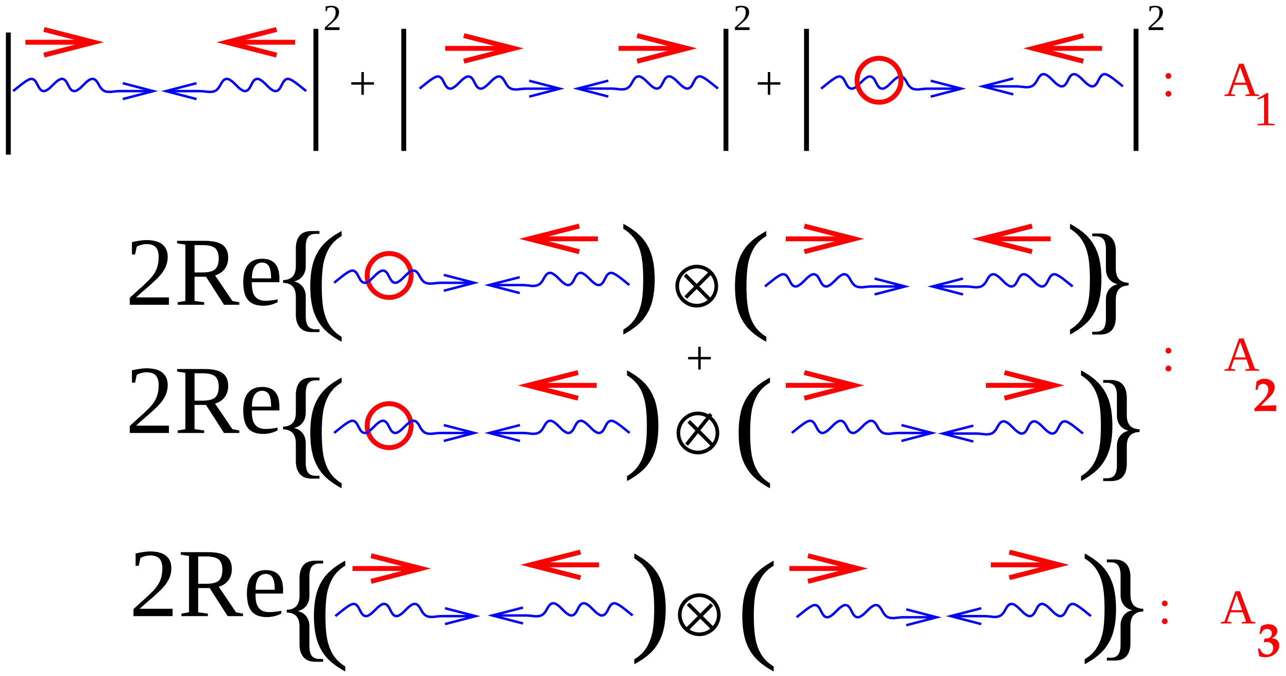

Figure 4: For a single-tag configuration, the target photons almost real and, in a very good approximation,purely transverse. There are only three possible independent helicity amplitudes. We show here, schematically,the relation between the coefficients A_i's and the possible helicity states, specified by the total photon helicity λ ($\lambda = 0, 1, 2$). Target photons are represented on the right and probe photons on the left.

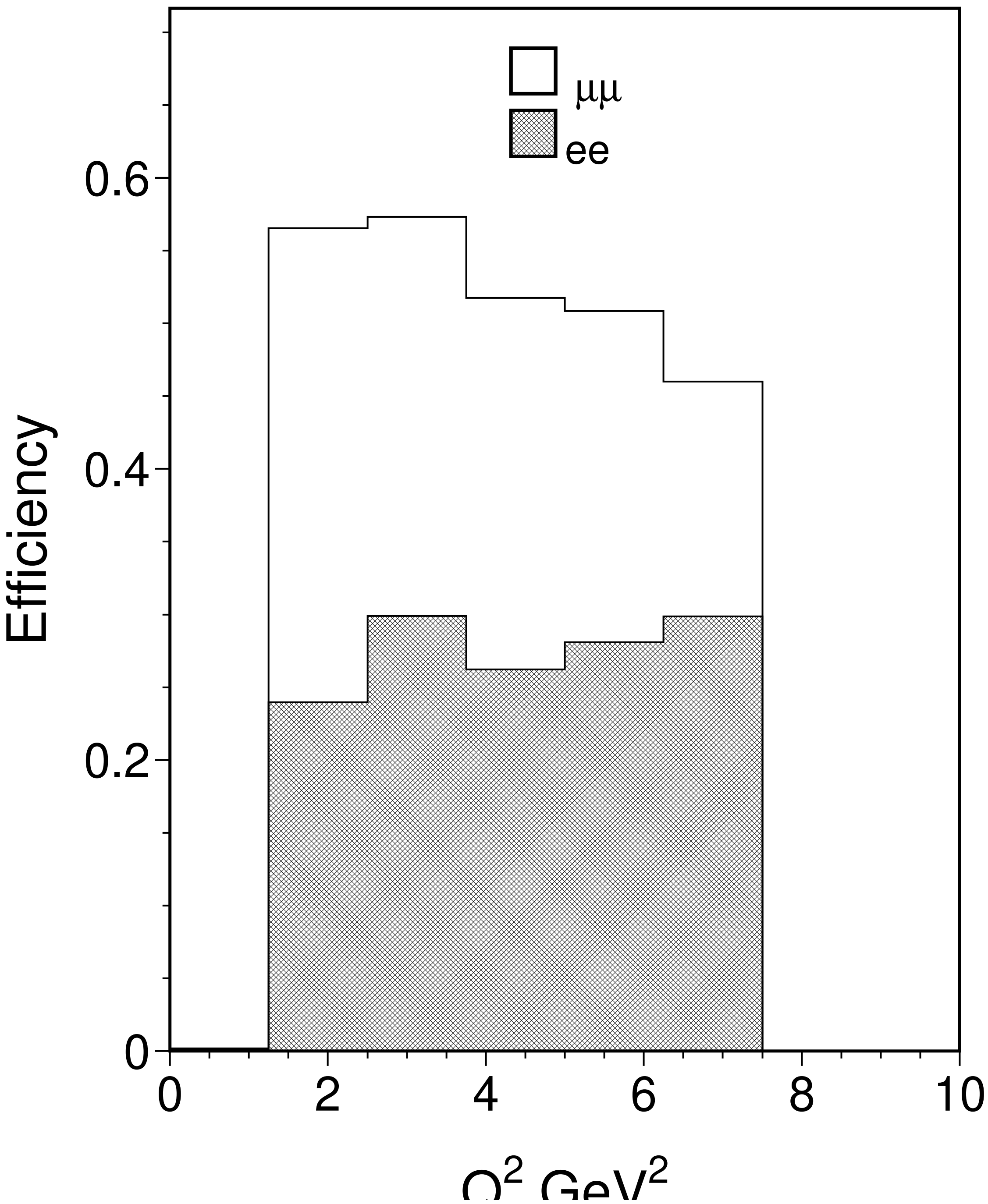

Figure 5: Selection efficiencies, for electrons and muons, in the studied Q^2 range.

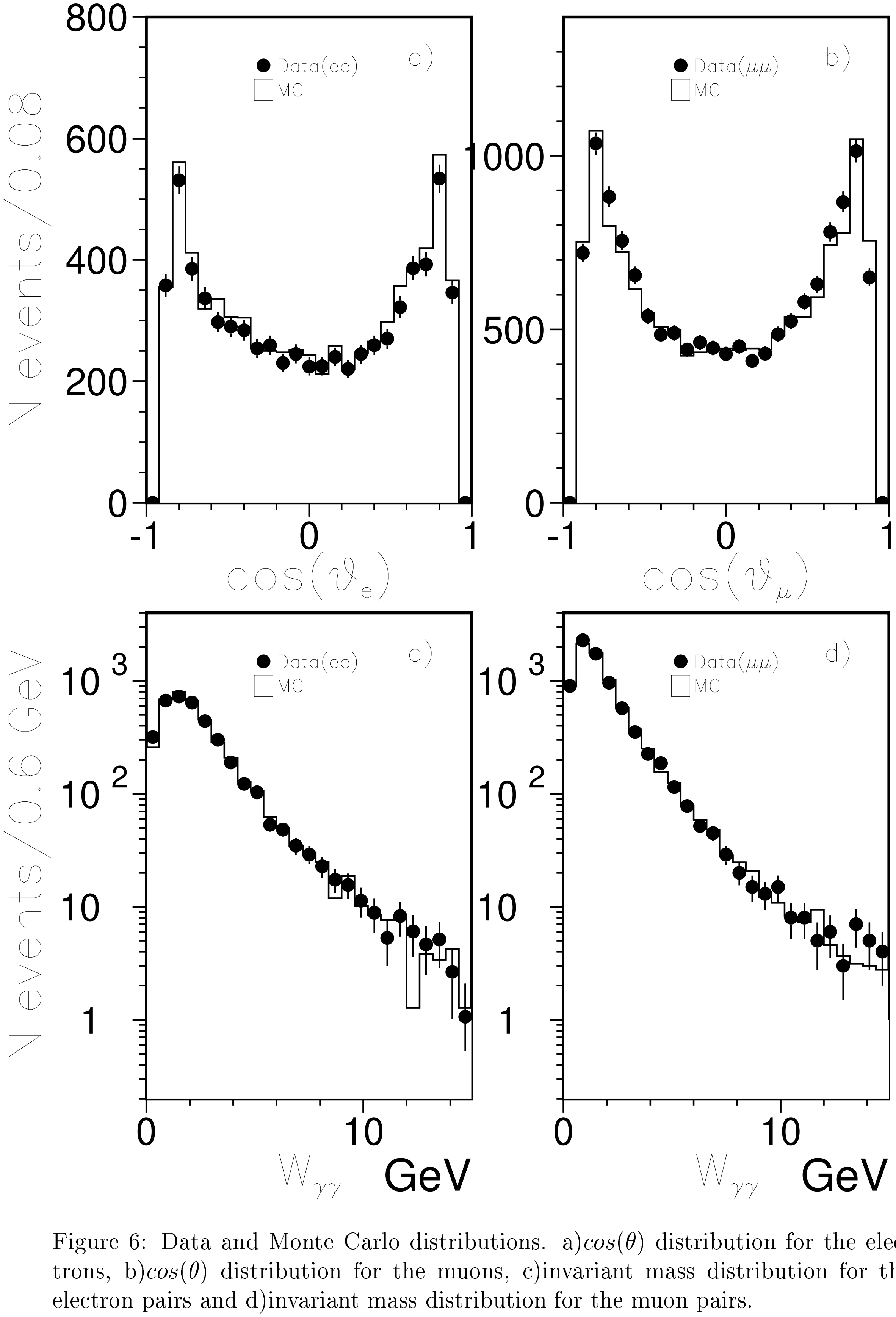

Figure 6: Data and Monte Carlo distributions. a)$cos(\theta)$ distribution for the electrons, b)$cos(\theta)$ distribution for the muons, c)invariant mass distribution for the electron pairs and d)invariant mass distribution for the muon pairs.

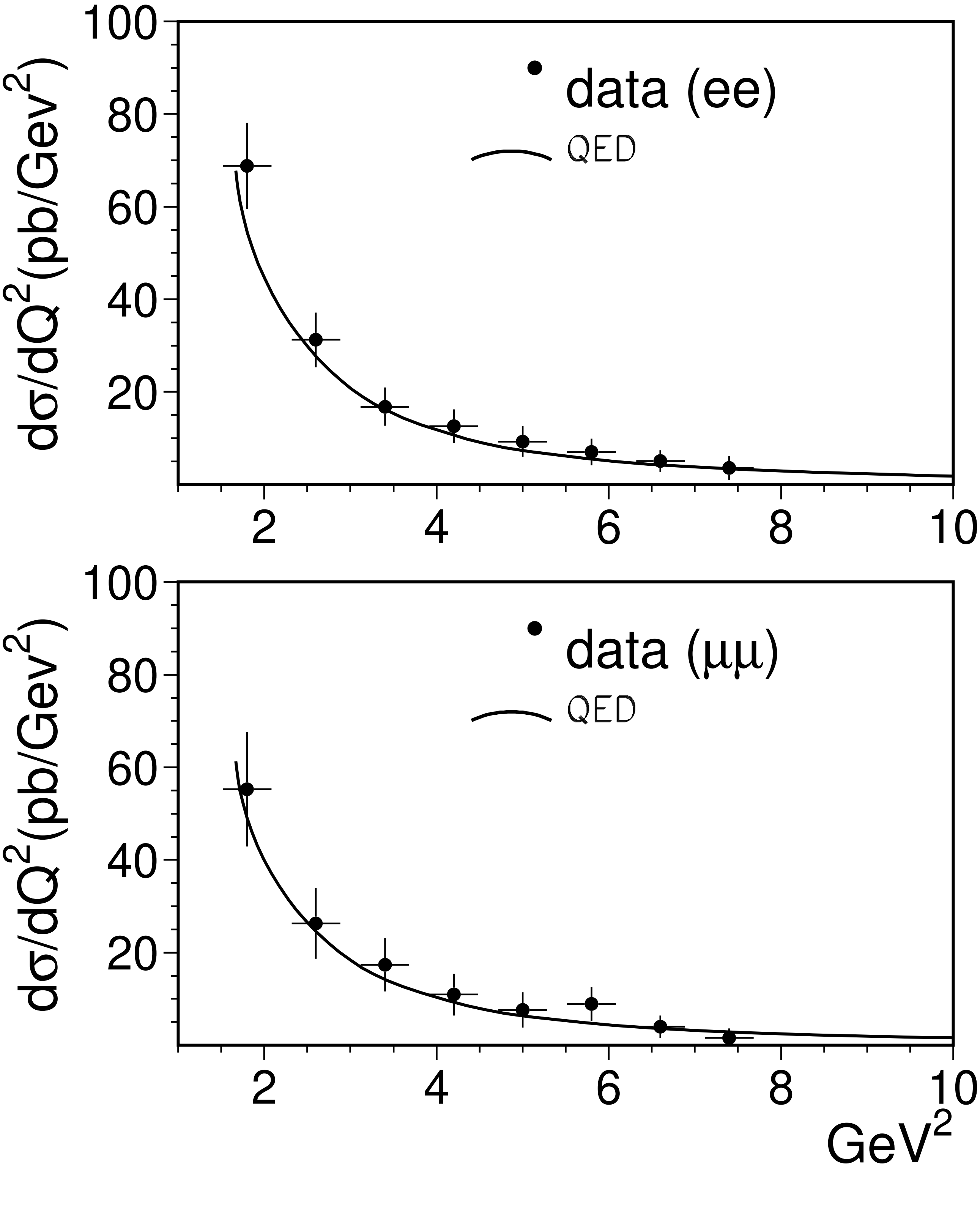

Figure 7: Cross section distribution as function of Q^2: the $eeee$ channel (upper plot). the $ee\mu\mu$ channel (lower plot). The QED curves have been obtained with a mean virtuality $t^2 = 0.033\ GeV^2$ for the target photon.

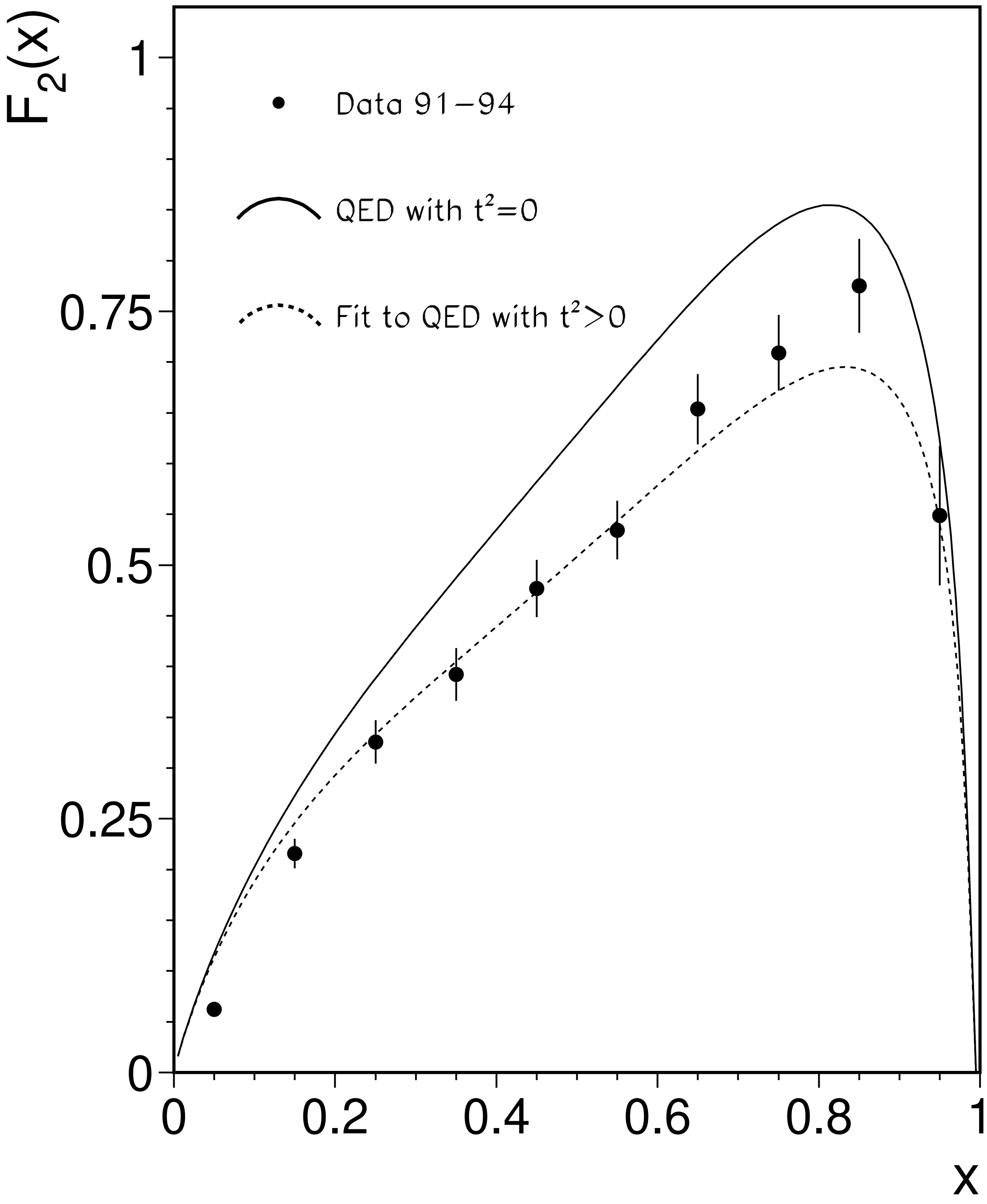

Figure 8: F_2^γ measured in the range $1.4\ GeV^2 \leq Q^2 \leq 7.6\ GeV^2$. The upper curve corresponds to $t^2 = 0$ while the lower curve is obtained by fitting the mean virtuality of the target photon to the data.

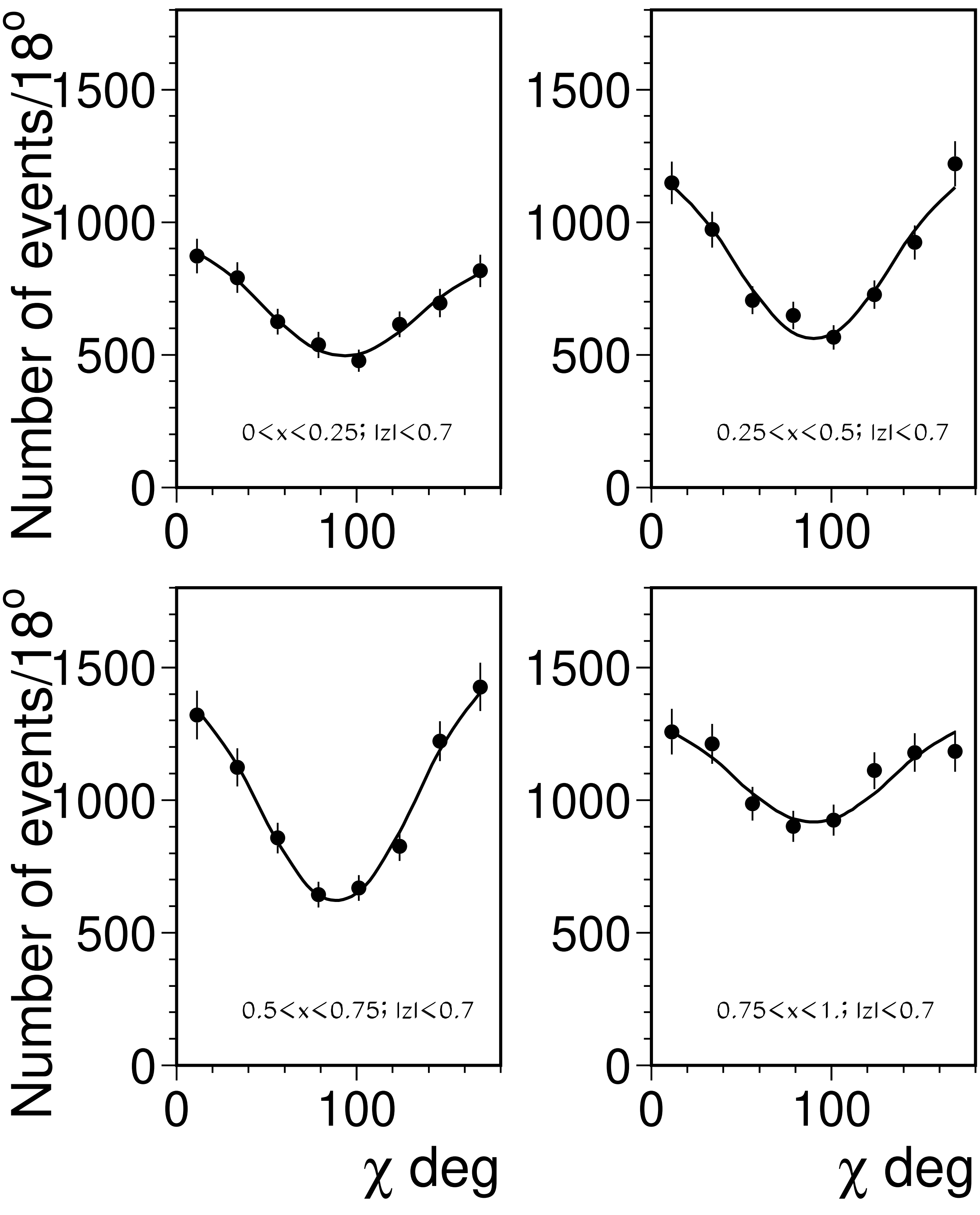

Figure 9: The four azimuthal distributions corresponding to the determination of $R_{2\chi}$.

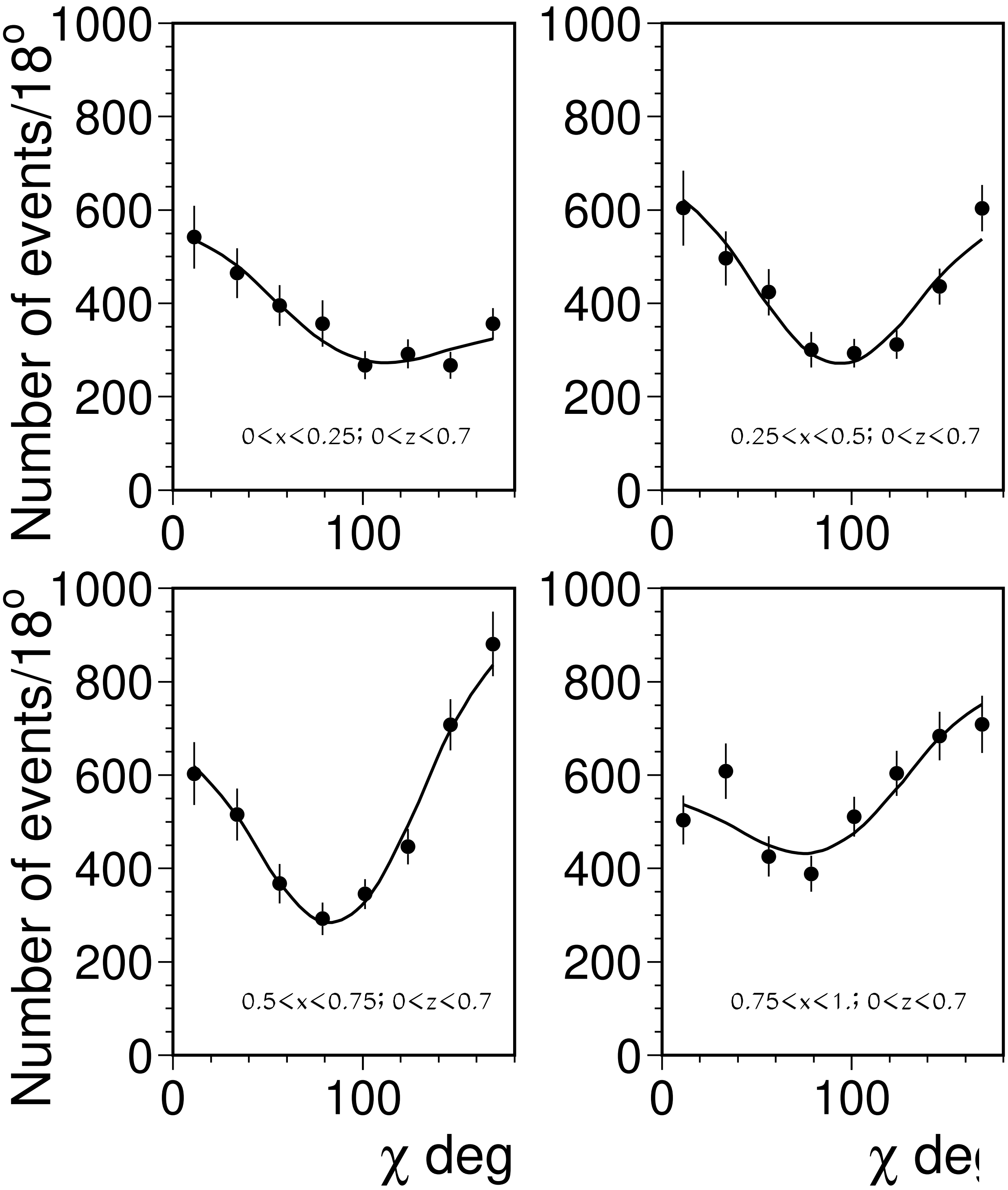

Figure 10: The four azimuthal distributions corresponding to the determination of R_χ for $z > 0$.

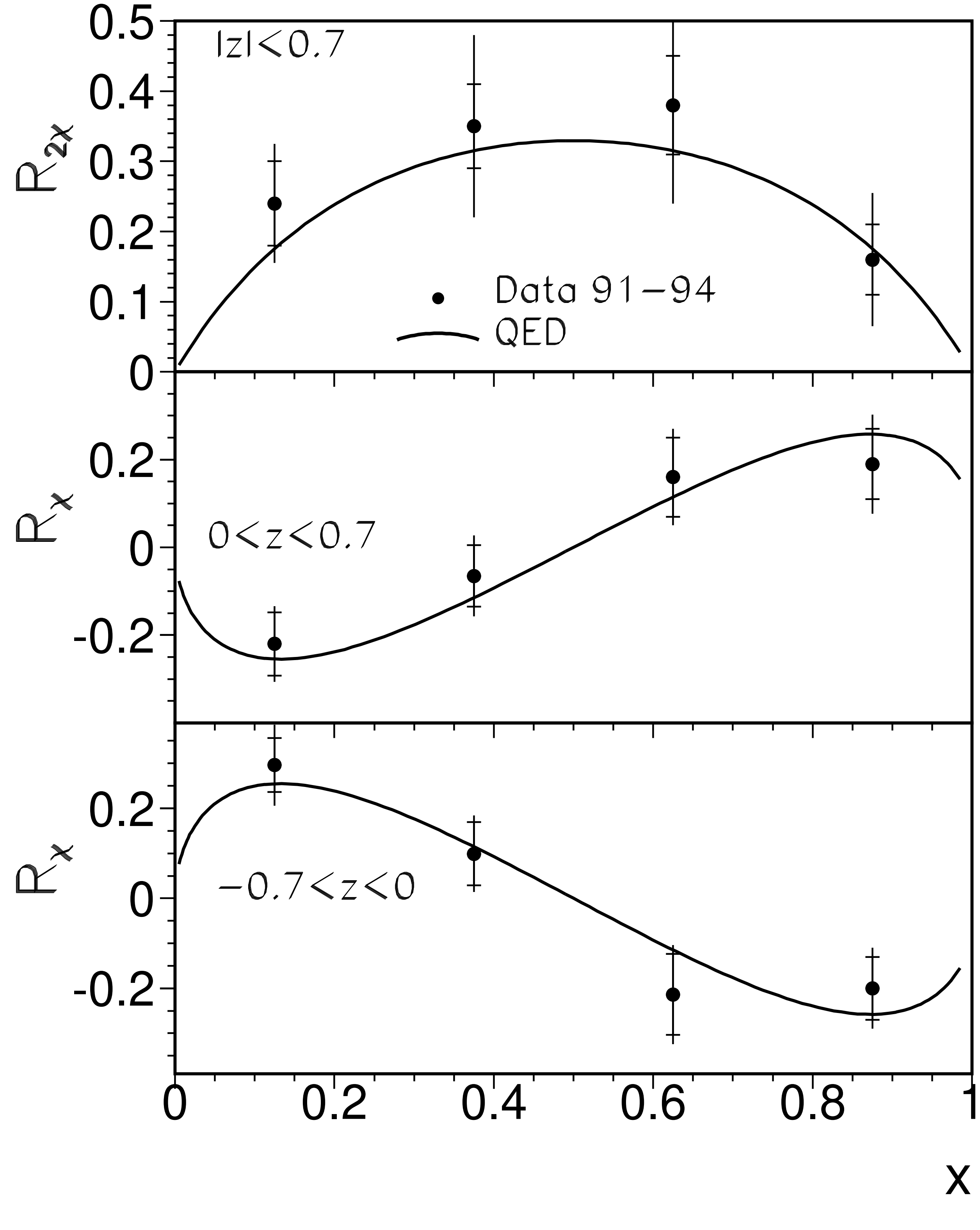

Figure 11: R_χ and $R_{2\chi}$ obtained values compared with the theoretical QED expectations. The outer error bars represents the sum, in quadrature, of the systematic and statistical (inner error bars) errors.

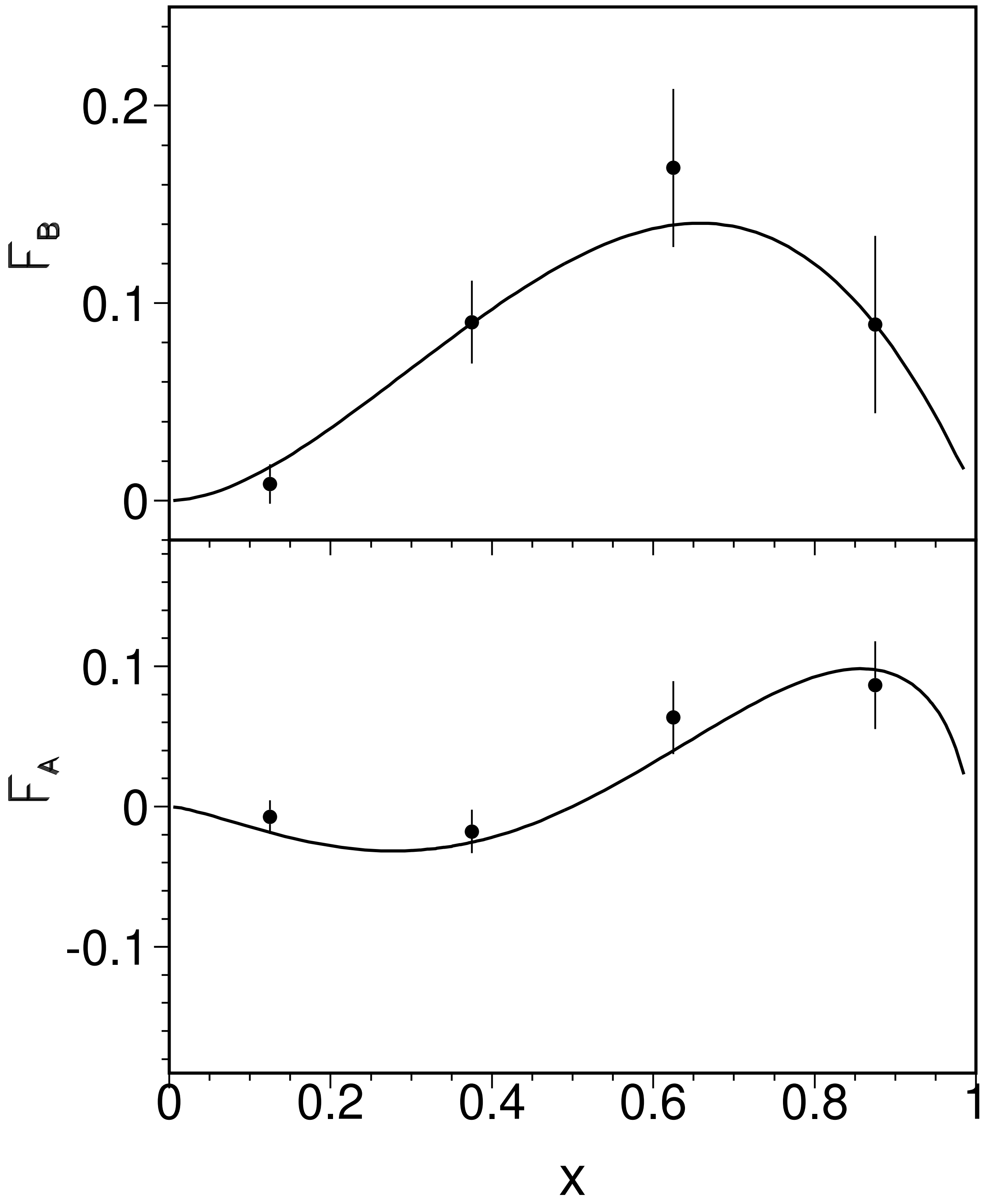

Figure 12: The structure functions F_B and F_A extracted from the R_χ, $R_{2\chi}$ and $F_2^{\gamma\gamma}$ determination. The structure function F_A represented here is the mean value between $F_A(z > 0)$ and $-F_A(z < 0)$.